

SPHEREx: Aromatics, Aliphatics and PAH Size across the Iris Nebula

C. BOERSMA ,¹ A. MARAGKOUAKIS ,¹ L.J. ALLAMANDOLA ,¹ J.D. BREGMAN ,¹ P. TEMI ,¹ V.J. ESPOSITO ,² AND R.C. FORTENBERRY ,³

¹ *NASA Ames Research Center, MS 245-6, Moffett Field, CA 94035-1000, USA*

² *Schmid College of Science and Technology, Chapman University, Orange, CA 92866, USA*

³ *Department of Chemistry & Biochemistry, University of Mississippi, University, MS 38677-1848, USA*

(Received October 23, 2025; Revised October 30, 2025; Revised December 5, 2025;

Accepted December 6, 2025)

Submitted to ApJ

ABSTRACT

Observations by the SpectroPhotometer for the History of the Universe, Epoch of Reionization, and Ices Explorer (SPHEREx) are combined with counterpart Spitzer spectral map data to study the aromatic, aliphatic, and PAH size evolution across the northwest photo-dissociation region (PDR) of the Iris Nebula (NGC7023). The 3.3–3.4 μm complex ($I_{3.3}$) and 11.2 μm ($I_{11.2}$) PAH band strength are determined through direct integration. In addition, the former is decomposed into a 3.3 ($I'_{3.3}$) and 3.4 μm ($I'_{3.4}$) sub-feature by fitting SPHEREx bandpass-integrated photometry using a modeled, highly sampled, multi-component spectrum. $I_{3.3}$, $I_{11.2}$, $I'_{3.3}$, and $I'_{3.4}$ all peak at the PDR. The NASA Ames PAH IR Spectroscopic Database is used to obtain the average number of carbon atoms ($\overline{N_C}$) and small PAH fraction (f_{small}) by fitting the isolated PAH component of the Spitzer segment; $70 \lesssim \overline{N_C} \lesssim 76$ and $0.24 \lesssim f_{\text{small}} \lesssim 0.36$. $I'_{3.4}/I'_{3.3}$, $I_{11.2}/I_{3.3}$, $\overline{N_C}$, and f_{small} all show a demarcation that matches the large-scale morphology of the region. For $I'_{3.3}$ and $I'_{3.4}$ this is reflected by two distinct trends when plotted against each other, one associated with the dense, the other with the diffuse medium; $[N_{\text{H,ali}}/N_{\text{H,aro}}]_{\text{dense}} = 0.42 \pm 0.01$ and $[N_{\text{H,ali}}/N_{\text{H,aro}}]_{\text{diffuse}} = 0.10 \pm 0.01$. $\overline{N_C}$ and f_{small} are tentatively correlated with $I_{11.2}/I_{3.3}$ ($R=0.54 \pm 0.05$ and -0.45 ± 0.05 , respectively). A wider variety of large(r) extended interstellar medium objects is required to tighten the correlations, turn them into quantitative calibrators for PAH size, and pin down the discrepancy of correlations with $I'_{3.3}$ involved.

Keywords: Polycyclic aromatic hydrocarbons (1280) — Near infrared astronomy (1093) — Interstellar molecules (849) — Laboratory astrophysics (2004) — Reflection nebulae (1381)

1. INTRODUCTION

Corresponding author: C. Boersma
 Email: Christiaan.Boersma@nasa.gov

The NASA Medium Class Explorer mission
 SpectroPhotometer for the History of the Uni-

verse, Epoch of Reionization, and Ices Explorer (SPHEREx; B. P. Crill et al. 2020) was successfully launched March 11, 2025. During its two-year mission it will be conducting the first near-infrared (IR), 0.75–5 μm , all-sky spectro-imaging survey at a spatial resolution of 6''.2. Emission from polycyclic aromatic hydrocarbons (PAHs) dominates the IR emission of many astronomical objects, including interstellar medium (ISM) sources in the Milky Way, nearby galaxies, and even high-redshift galaxies (A. G. G. M. Tielens 2008; J. Spilker et al. 2023). The blended 3.3 and 3.4 μm emission band complex is a prominent PAH feature covered by SPHEREx. Its potential to study the 3.3 and related 3.4 μm components was recently explored by E. Zhang et al. (2025) and Y.-T. Cheng et al. (2025). Obtaining 3.3 μm measurements of local interstellar medium (ISM) sources, especially those that are extended in nature, can provide valuable information on the evolution of the PAH aliphatic/aromatic ratio as well as PAH size (e.g., L. J. Allamandola et al. 1989; A. Li & B. T. Draine 2012; X. J. Yang et al. 2017). In particular with the 3.4/3.3 and 11.2/3.3 μm PAH band strength ratios, where the former traces the aliphatic/aromatic ratio and the latter is considered the ultimate tracer for PAH size (see e.g., A. Maragkoudakis et al. 2020).

SPHEREx’s spatial-spectral characteristics are well-paired with those of the Infrared Spectrograph (IRS; J. R. Houck et al. 2004) instrument onboard NASA’s Spitzer Space Telescope (M. W. Werner et al. 2004). When used in its spectral mapping mode, Spitzer observations, which start at 5.2 μm , can be extended down into the near-IR at comparable spatial and spectral resolution with SPHEREx data. The goal of this work is to perform such an analysis and study the aromatic, aliphatic, and PAH size evolution across the Iris Nebula (NGC7023), a reflection nebula (RN) located in

Cepheus. NGC7023 is irradiated by HD200775, a B2Ve (C. Rogers et al. 1995) massive spectroscopic binary (R. Millan-Gabet et al. 2001) Herbig Be star. HD200775 is 430 pc away (M. E. van den Ancker et al. 1997). Figure 1 depicts NGC7023’s northwest photo-dissociation region (PDR). The PAH emission in this PDR has been extensively studied (e.g., O. Berné et al. 2007; M. J. F. Rosenberg et al. 2011; P. Pilloni et al. 2012; C. Boersma et al. 2013, 2014a, 2015, 2016; D. J. Stock et al. 2016; B. A. Croiset et al. 2016; C. Boersma et al. 2018; K. Misselt et al. 2025). SPHEREx opens up a new opportunity to study the large-scale evolution of the aliphatic/aromatic ratio and PAH size across NGC7023.

2. OBSERVATIONS AND DATA REDUCTION

Spitzer spectral map data on NGC7023 have been taken from C. Boersma et al. (2018) and the reader is directed there for details on its reduction. The `astroquery` Irsa-interface was used to retrieve Multi-Extension FITS (MEF) images that have pixels overlapping the Spitzer spectral cube’s field-of-view (FOV) from the SPHEREx Archive at the NASA/IPAC Infrared Science Archive (IRSA; SPHEREx Team 2025). These data are from the SPHEREx Quick Release 2 (QR2) and consist of observations from Survey 1 with Header Data Unit (HDU) creation dates spanning 2025-09-15 to 2025-09-19.

The calibrated surface brightness is provided in MJy/sr as 2040 \times 2040 pixel images with accompanying variances and predictions of the zodiacal light. Spectral coverage is from 0.75–5 μm at a resolution R ($\equiv \lambda/\Delta\lambda$) of 41–130.

`photutils` was used for spectral extraction, after subtracting out the predicted zodiacal light. To match the Spitzer with the SPHEREx observations, 2 \times 2 spatial pixels of the IRS map

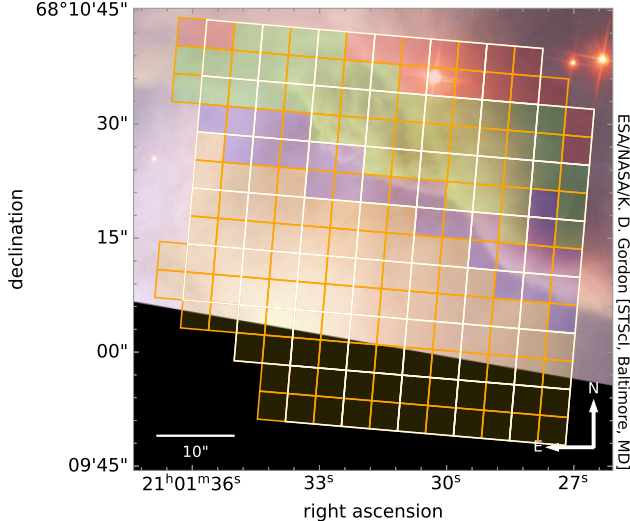


Figure 1. Composite Hubble Space Telescope ACS image of the northwest photo-dissociation region (PDR) in the reflection nebula NGC7023. Combined H α and infrared I-band data are shown in red, optical V-band data in green, and optical B-band data in blue. The irradiating star HD200775 is located some 43" from the center of the image toward the southeast, just outside the field of view. In orange Spitzer-IRS spectral map pixels are shown. Superimposed are four zones, colored red, green blue, and yellow, that were identified through hierarchical clustering of the Spitzer spectra, see C. Boersma et al. (2018) for details. Blue marks the PDR-front, which forms the boundary between the dense medium toward the north from the diffuse medium in the south. Matching SPHEREx spectral extraction apertures are shown in white.

were combined¹, resulting in a 7×7 spectral map with a pixel size of 7".2 \times 7".2, see Figure 1. Associated uncertainties were determined by performing the same extraction on the variance maps and subsequently taking the square root.

Since SPHEREx is a spectro-photometer that utilizes a linear variable filter, each detector pixel has its own associated wavelength and

¹ The spectral map of NGC7023 from C. Boersma et al. (2018) has already a 2×2 spatial resampling applied. Therefore, each SPHEREx aperture matches 4×4 native spatial Spitzer pixels.

bandwidth. A mapping is provided in the MEF files. Wavelength and width are assigned to each extracted spectral data point by averaging the values assigned to each SPHEREx pixel in the aperture, weighted with the overlap of the pixel with the aperture.

`pyphot` was used to predict Spitzer-IRAC channel 1 photometry from the extracted SPHEREx segment and IRAC channel 4 photometry from the 2×2 resampled Spitzer segment to facilitate splicing. IRAC 1 and 4 Spitzer Enhanced Imaging Products (SEIP) Super Mosaics for NGC7023 were obtained from the Spitzer Heritage Archive (SHA) at IRS. The mean mosaics were used in combination with `photutils` to retrieve matching photometric measurements for each of the SPHEREx apertures in Figure 1.

Figure 2 presents the extracted SPHEREx and Spitzer segments at the center pixel of the constructed spectral cube. The IRAC band-passes are indicated as well as the predicted channel 1 and 4 photometry.

3. ANALYSIS

To study the aliphatic/aromatic ratio and PAH size evolution across the northwest PDR in NGC7023 through the 3.4/3.3 and 11.2/3.3 μm PAH band strength ratios, respectively, the 3.3, 3.4, and 11.2 μm PAH band strengths must be determined. This is done on extinction-corrected spectra, detailed in Appendix A, with measurements on the SPHEREx segment scaled to match the relative predicted and observed IRAC photometry, which is detailed in Appendix B. Two methods are used to determine these band strengths.

3.1. Direct Band Measurements

The most straightforward way to determine PAH band strengths is through direct integration. Here, the PAH feature is isolated after subtracting a straight baseline with two anchor points. For the 3.3–3.4 μm PAH band com-

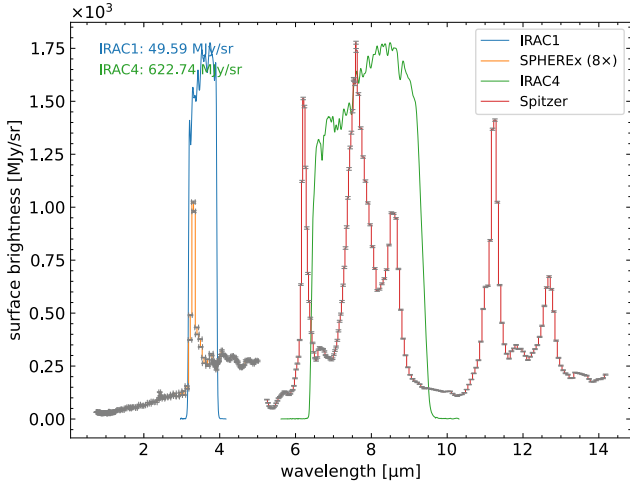


Figure 2. Extracted SPHEREx and resampled Spitzer segments for the center pixel of the 7×7 constructed spectral cube, see Figure 1. To highlight the SPHEREx segment, it is multiplied $8 \times$. Uncertainties are indicated with the gray vertical error bars. For the SPHEREx segment, horizontal error bars represent the bandpass of each spectro-photometric data point. IRAC channel 1 (blue) and 4 (green) bandpasses have been indicated as well as their predicted photometry.

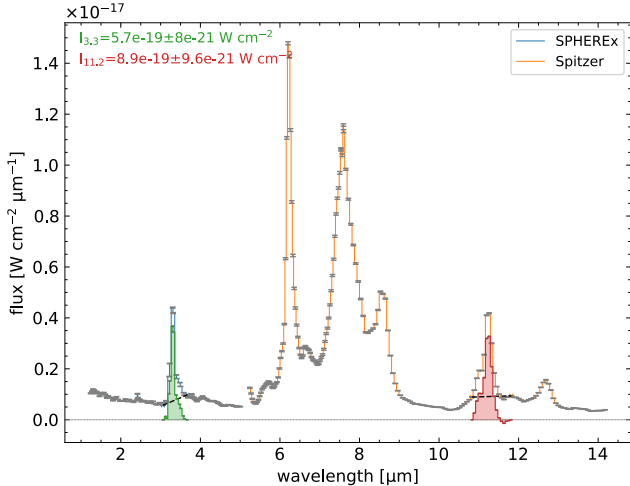


Figure 3. PAH band strength determination through direct integration. A straight baseline (dashed black) is drawn and subtracted to isolate the 3.3–3.4 μm complex (green) and 11.2 μm (red) PAH band. Uncertainties are indicated as gray error bars. The derived PAH band strengths and their uncertainty are indicated. See Section 3.1 for details.

plex, these are 3.07 and 3.65 μm and for the 11.2 μm PAH band 10.8 and 11.8 μm . Band strength uncertainties are determined by direct integration of the variance and taking a subsequent square root. Figure 3 demonstrates this approach for the center pixel of the 7×7 constructed SPHEREx+Spitzer spectral cube of NGC7023.

3.2. Spectro-photometric Modeled Band Determination

Alternatively, the SPHEREx observations can be fully treated as photometric data points. This has the advantage of being able to separate out the blended 3.3 and 3.4 μm features, which is otherwise difficult to achieve given SPHEREx’s spectral resolution. The 3.3 and 3.4 μm features are commonly attributed to aromatic and aliphatic C-H stretches, respectively (e.g., L. J. Allamandola et al. 1989; A. Li & B. T. Draine 2001).

In this approach the spectro-photometric SPHEREx observations are reproduced by fitting the bandpass-integrated photometry using the highly sampled spectral model that is described in Appendix C.

`astropy`’s modeling framework is used to implement the model, in combination with its `TRFLSQFitter` fitter. Figure 4 presents the results for the SPHEREx segment of the central pixel of the spectral cube. The left panel of the figure compares the observed bandpass-integrated photometry versus its modeled counterpart. In the figure’s right panel, the highly sampled spectrum is overlaid atop the SPHEREx segment, indicating each of the spectral components and determined band strengths.

4. RESULTS AND DISCUSSION

Maps of the determined 3.3, 3.4, and 11.2 μm band strengths are presented in Figure 5. The top two panels show those established through direct integration whereas the bottom two those

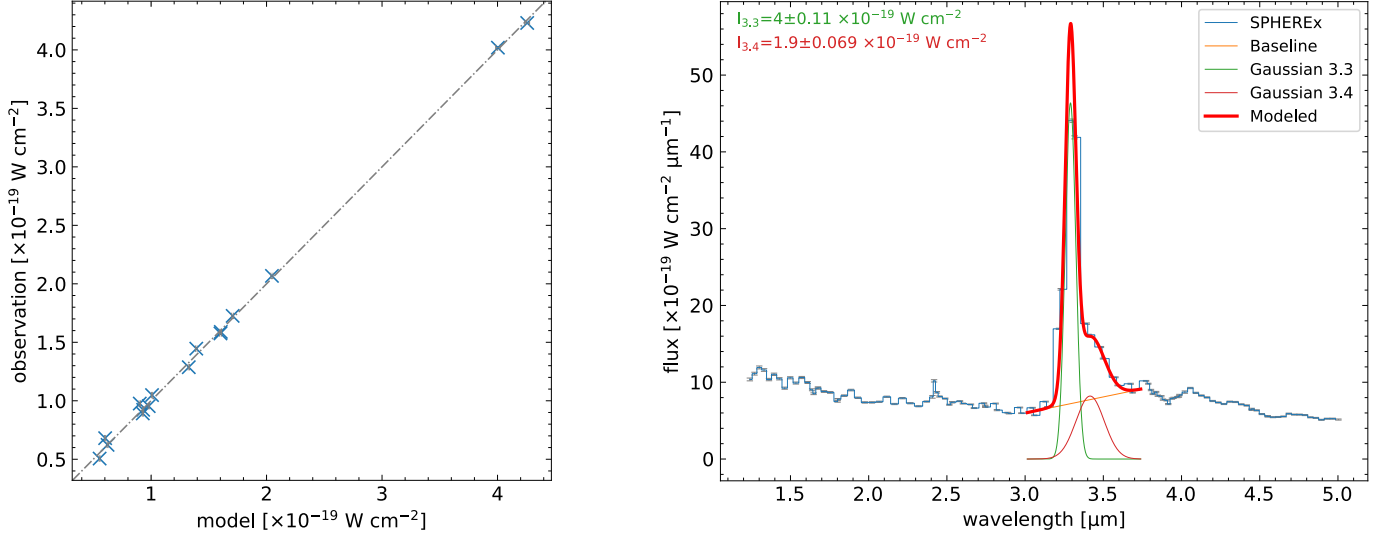


Figure 4. Left: Observed versus modeled SPHEREx bandpass-integrated photometry for the central pixel of the 7×7 constructed spectral cube, see Fig. 1. The dashed-dotted line shows the one-to-one line. Right: Modeled, highly sampled 3.3–3.4 μm complex (red) overlaid atop the observed SPHEREx segment (blue). Also shown are the individual 3.3 (green) and 3.4 μm (maroon) component as well as the determined baseline (orange). Uncertainties are indicated as gray error bars. Derived band strengths and their uncertainties are given as well. See Section 3.2 for details.

from the spectro-photometric modeling. A distinction is made between either approach by decorating the latter with a quote “”, i.e., $I_{3.3}$ versus $I'_{3.3}$, respectively. Note that the maps of $I_{3.3}$, $I'_{3.3}$, and $I'_{3.4}$ have the scaling factors from Appendix B applied.

4.1. The Spectra

Focusing on the SPHEREx segment, Figures 2, 3, and 4 clearly show the 3.3–3.4 μm PAH complex, which is made up of the blended 3.3 and 3.4 μm sub-features. A jump is seen around 3 μm that persists beyond the 3.3–3.4 μm PAH complex up to $\sim 4.4 \mu\text{m}$ with signs of substructure at 3.8, 4.0, and 4.4 μm . This broad band emission has been attributed to a quasi PAH continuum, ascribed to 2-quanta combination bands and overtones of the strong PAH fundamental bands in the 5–15 μm region (L. J. Allamandola et al. 1989; C. Boersma et al. 2023; V. J. Esposito et al. 2023).

A stellar component, best visible in the F_{λ} - λ spectra of Figures 3 and 4, is also evident. It is particularly prominent in the northwest corner

of the FOV, where an embedded young stellar object (YSO) is located, see Figure 1.

4.2. The Maps

The maps in Figure 5 show a clear demarcation between the dense and diffuse medium toward the north and south of the FOV, respectively, that matches the morphology apparent in Figure 1. At the PDR, the emission peaks and gradually falls off when crossing into the diffuse medium and when nearing the embedded YSO located toward the northwest.

The morphologies of the 3.3, 3.4, and 11.2 μm maps match up well. This is expected due to their common origin in C-H vibrational modes. The 11.2 μm map mirrors that from C. Boersma et al. (2014a), albeit at a coarser spatial resolution. There is no sign of the arc that can be discerned in some of the PAH band strength maps from C. Boersma et al. (2014a; their Figure 5), and that is faintly visible in Figure 1. K. Misselt et al. (2025) report an offset between the peak of the aromatic $I'_{3.3}$ and aliphatic $I'_{3.4}$ emission in high spectral-spatial resolution James Webb

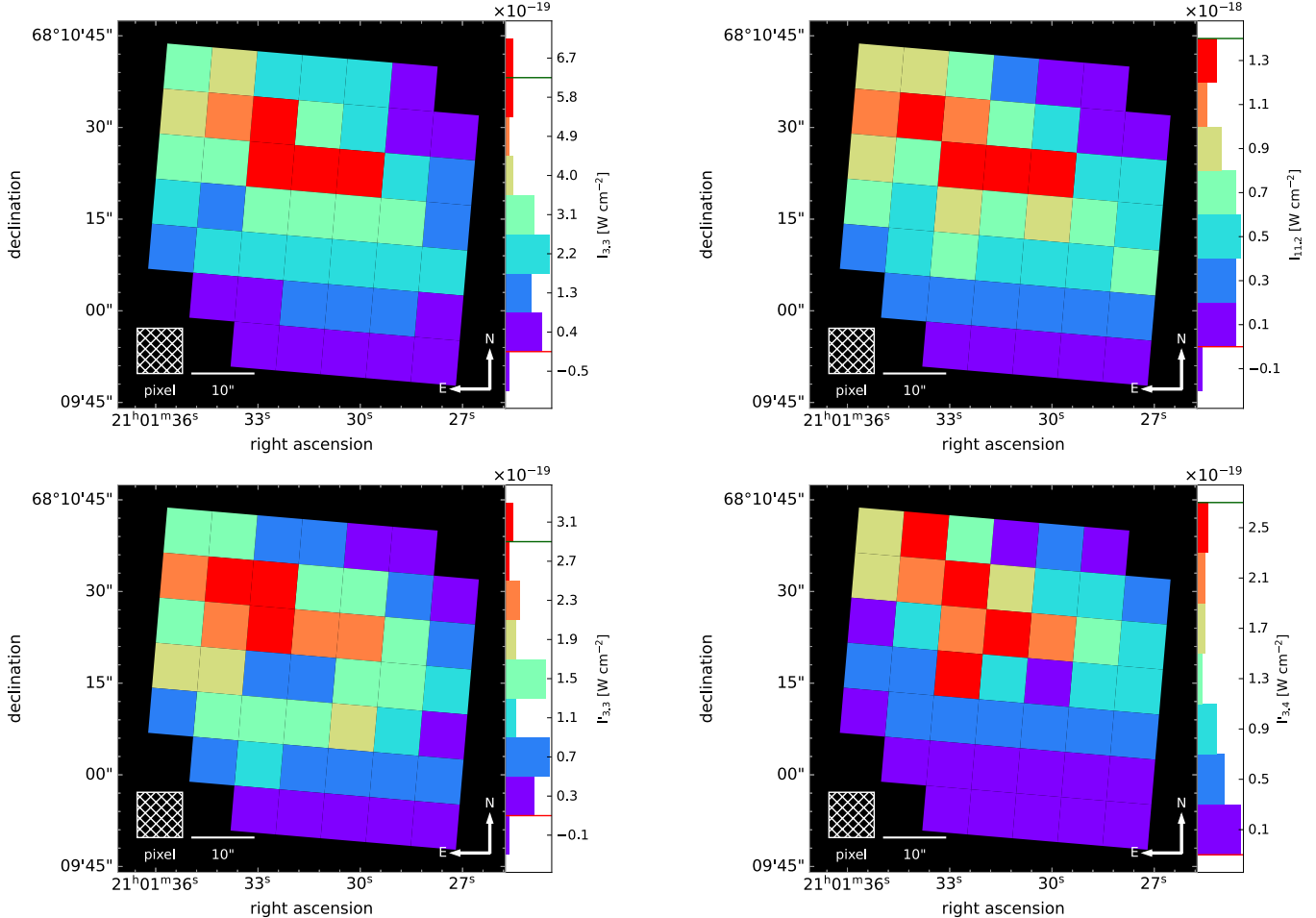


Figure 5. Maps of the northwest PDR in NGC7023 in the PAH 3.3–3.4 μm complex, 3.3, 3.4 and 11.2 μm bands. Top: 3.3–3.4 μm complex and 11.2 μm band strengths determined through direct measurement. See Section 3.1 for details. Bottom: 3.3 and 3.4 μm band strength determined using a multi-component photometric decomposition. See Section 3.2 for details. The color scales use a 4% cutoff on the high and a 1% cutoff on the low end, indicated by the green and red lines in the color bar, respectively. This suppresses outliers. See Section 4 for details.

Space Telescope (JWST; J. P. Gardner et al. 2006) observations that is not resolved here.

4.3. The 3.4/3.3 μm Band Strength Ratio

The left panel of Figure 6 presents a map of the $I'_{3.4}/I'_{3.3}$ band strength ratio, where the numerator traces aliphatic and the denominator aromatic carbonaceous material (PAHs). Apart from some ‘hot’ pixels, there is a clear demarcation between the dense and diffuse region, with the ratio systematically higher in the former.

Plotting $I'_{3.4}$ versus $I'_{3.3}$ in the right panel of Figure 6 reveals a bifurcation that matches with

what is observed in the left panel. This is best seen when color coding each point according their zone assignment from Figure 1, which is based on hierarchical clustering of the Spitzer spectra (C. Boersma et al. 2018). Points associated with the diffuse (yellow) and dense medium (green) make up two distinct trends. Similar behavior has been observed for the 11.2 versus 8.6 μm PAH band strength (C. Boersma et al. 2015, 2016, 2018) for NGC7023, which was related to an evolution in PAH charge. B. Khan et al. (2025) observed branching in some of their correlation plots involving the 8.6 μm PAH band

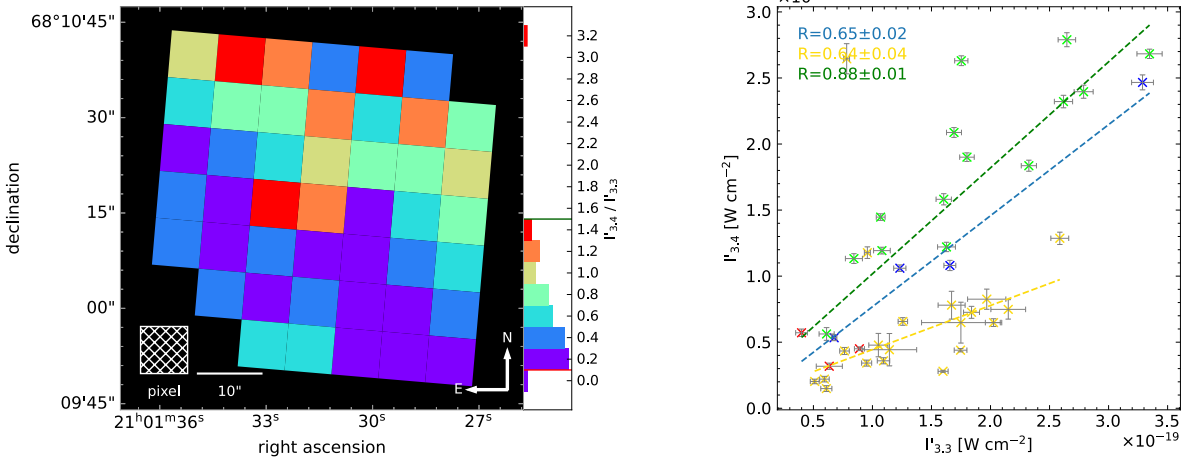


Figure 6. Left: Map of the northwest PDR in NGC7023 in the 3.4/3.3 μm band strength ratio, derived using spectro-photometric modeling. The color scale uses a 4% cutoff on the high and a 1% cutoff on the low end, indicated by the green and red lines in the color bar, respectively. This suppresses outliers. Right: $I'_{3.4}$ versus $I'_{3.3}$. Points are color coded according their zone as assigned in Figure 1. Uncertainties have been propagated, indicated as gray error bars, and points with a SNR less than three have been discarded. Given are the weighted Pearson correlation coefficients R for a straight line (dashed) associated with all data (blue), the diffuse medium (yellow), and the dense medium (green). See Section 4.3 for details.

in JWST observations of the Orion Bar. These authors conclude that only a subset of the interstellar PAH family contribute to the 8.6 μm PAH band and, subsequently, attribute them to changes in PAH size.

As far as $I'_{3.4}/I'_{3.3}$ is concerned, its evolution across the northwest PDR of NGC7023 is consistent with an interpretation that aliphatic hydrogen side groups have a better chance of surviving in more shielded, denser regions but, once exposed, are rapidly photo-dissociated from the parent PAH. This includes both superhydrogenated and methylated PAHs, where the former have been shown to produce a better match with observations (M. P. Bernstein et al. 1996; S. A. Sandford et al. 2013; X. J. Yang et al. 2020). Experiments suggest that PAHs with different side groups are released from ices at the PDR-front, where their production and residence time in the ice has promoted superhydrogenation and the addition of side groups (C. X. Mendoza-Gomez et al. 1995; M. P. Bernstein et al. 1999, 2002)

Following X. J. Yang & A. Li (2023), the ratio of the number of aliphatic ($N_{\text{H,ali}}$) relative to aromatic ($N_{\text{H,aro}}$) hydrogens in the dense and diffuse medium is found to be $[N_{\text{H,ali}}/N_{\text{H,aro}}]_{\text{dense}} = 0.42 \pm 0.01$ and $[N_{\text{H,ali}}/N_{\text{H,aro}}]_{\text{diffuse}} = 0.10 \pm 0.01$, respectively. The latter value is somewhat consistent with that found by K. Misselt et al. (2025; $0.062 \lesssim N_{\text{H,ali}}/N_{\text{H,aro}} \lesssim 0.23$) from JWST observations centered on the peak of the PAH emission at the PDR-front. Though, the previous value for the dense medium is higher by a factor of two. This difference is attributed, in part, to the FOV considered here being much larger ($50''.4 \times 50''.4$ versus $\sim 3''.3 \times 21''$) and extending further into the more shielded, molecular regions. Moreover, the entire JWST FOV is covered by a mere $\sim 0.5 \times 3$ SPHEREx+Spitzer pixels. In addition, because of the two orders of magnitude difference in spectral resolution, K. Misselt et al. (2025) are able to isolate the 3.3 and 3.4 μm features from each other and any other components far more carefully, which impacts the determined band strengths.

4.4. The 11.2/3.3 μm Band Strength Ratio

Figure 7 presents maps of the 11.2/3.3 μm PAH band strength ratio. The figure's left panel uses the 3.3 μm band strength determined through direct integration ($I_{3.3}$; Section 3.1) while the right panel that derived from the spectro-photometric modeling ($I'_{3.3}$; Section 3.2).

The 11.2/3.3 μm PAH band strength ratio has been shown to be an important tracer for PAH size (e.g., L. J. Allamandola et al. 1989; A. Maragkoudakis et al. 2020; B. T. Draine et al. 2021; A. Maragkoudakis et al. 2023). At face value, the survivability of smaller PAHs is expected to decrease when moving from the shielded dense medium into the exposed diffuse medium, mirroring the behavior of $I'_{3.4}/I'_{3.3}$ in Figure 6. Indeed, the left panel of Figure 7 shows a clear demarcation with smaller PAHs, i.e., smaller 11.2/3.3 ratios, more prominent across the dense medium. This is consistent with results from B. A. Croiset et al. (2016) that are based on a combination of Stratospheric Observatory For Infrared Astronomy (SOFIA; E. T. Young et al. 2012) FLITECAM and FORCAST observations.

However, the right panel of Figure 7, which replaces $I_{3.3}$ with $I'_{3.3}$, paints a different, far more chaotic picture. Gone are the clear demarcation and the smooth transition between the dense and diffuse medium when crossing the PDR-front. This difference could be due to a reduction in signal quality, but the dynamic ranges, 6.3 versus 4, remain comparable. Arguably, limitations of the spectro-photometric model used to isolate the 3.3 μm feature from the 3.4 μm sub-feature could be the cause. For example, the model described in Appendix C combines the 3.4 μm feature and underlying plateau that is shared with the 3.3 μm feature into a single Gaussian. Nevertheless, the 3.4/3.3 μm results do demonstrate merit for this approach.

Recent work (V. J. Esposito et al. 2024) has shown that the distinction between aliphatic and aromatic C-H stretch features is not as clear cut as previously thought. This, in combination with the above, could also be a contributing factor for the observed differences when using $I'_{3.3}$ in the ratio.

4.5. The PAH Size Evolution across NGC7023

To obtain a quantitative measure for the evolution of PAH size across NGC7023, the NASA Ames PAH IR Spectroscopic Database (PAHdb hereafter; C. W. Bauschlicher et al. 2010; C. Boersma et al. 2014b; C. W. Bauschlicher et al. 2018; A. L. Mattioda et al. 2020) is employed to fit the 5.2–15 μm isolated, extinction corrected Spitzer PAH segment of the spectra. This approach is largely analogous to that used by C. Boersma et al. (2013, 2015, 2016, 2018), the main differences being: 1. the use of a much more recent version (4.00- α ; A. Maragkoudakis et al. 2025) of PAHdb's library of computed PAH spectra, 2. exclusion of nitrogen containing PAHs (PANHs; per A. Ricca et al. 2024), 3. no application of an emission redshift (per C. J. Mackie et al. 2018), 4. incorporating an excitation energy of 7 eV, and 5. having Gaussian line profiles with a fixed full-width at half maximum (FWHM) of 15 cm^{-1} . This matches the optimal PAHdb modeling configuration from A. Maragkoudakis et al. (2025). A Monte Carlo approach is taken where the spectra are varied within their uncertainties 1024 times and fitted to obtain a statistical measure, i.e., mean and standard deviation, for derived parameters². The interaction with the library, emission modeling, and fitting are done with PAHdb's suite of Python tools³ (The PAHdb Team 2022).

² These do not capture uncertainties associated with the PAHdb spectra or the emission modeling, neither statistical nor systematic.

³ github.com/PAHdb/AmesPAHdbPythonSuite

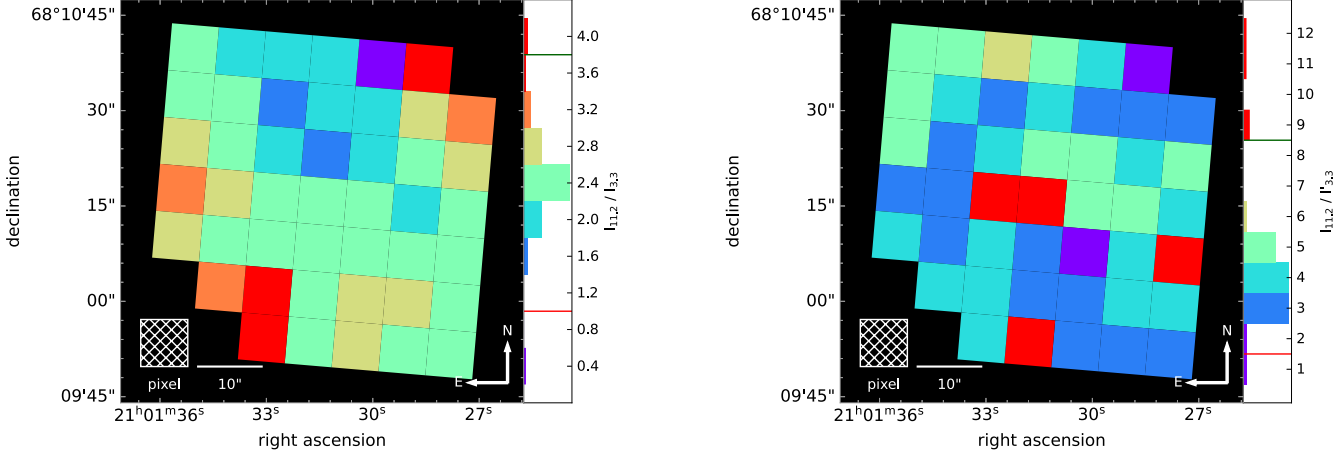


Figure 7. Maps of the northwest PDR in NGC7023 in the 11.2/3.3 μm PAH band strength ratio. The 3.3 μm band strength determined through direct integration ($I_{3.3}$) and spectro-photometric modeling ($I'_3.3$) are presented in the left and right panel, respectively. The color scales use a 4% cutoff on the high and a 1% cutoff on the low end, indicated by the green and red lines in the color bar, respectively. This suppresses outliers. See Section 4.4 for details

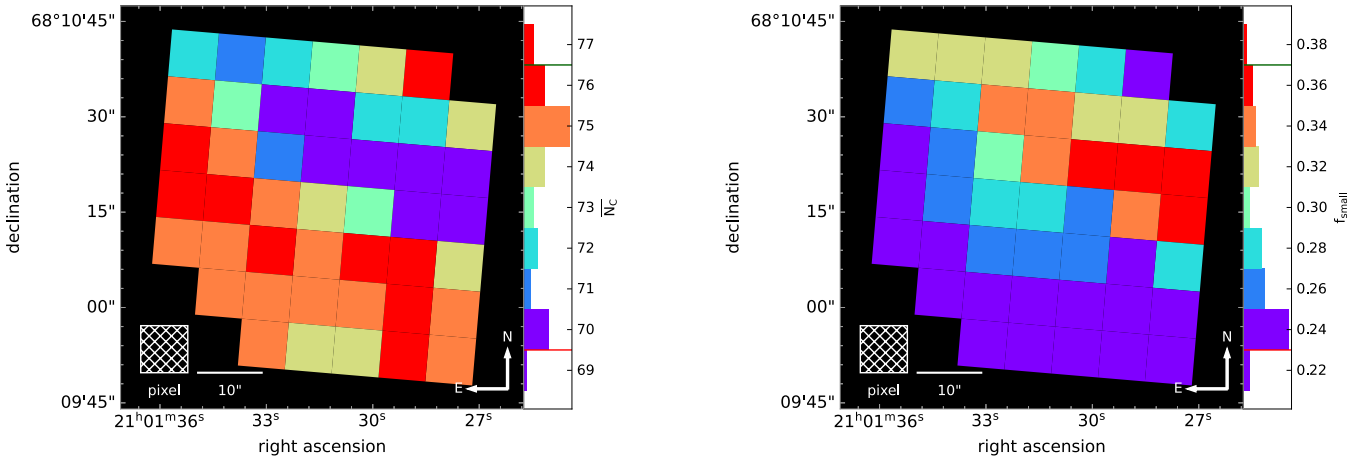


Figure 8. Maps of the northwest PDR in NGC7023 showing the average number of carbon atoms ($\overline{N_C}$; left) and small PAH fraction (f_{small} ; $N_C \leq 50$; right) determined from a Monte Carlo PAHdb-fit to each pixel's corresponding Spitzer segment isolated PAH spectrum. The color scales use a 4% cutoff on the high and a 1% cutoff on the low end, indicated by the green and red lines in the color bar, respectively. This suppresses outliers. See Section 4.5 for details.

Figure 8 presents maps of the determined average number of carbon atoms $\overline{N_C}$ and small PAH fraction f_{small} ($N_C \leq 50$). Despite their limited span, especially for $\overline{N_C}$ ($\sim 70\text{--}76$), both maps pick up the demarcation between the dense and diffuse medium toward the north and south of the FOV, respectively. As expected, $\overline{N_C}$ increases and f_{small} drops across the PDR

and into the diffuse medium. Compared to B. A. Croiset et al. (2016), who find on average $N_C \simeq 70$ in the diffuse medium and ~ 50 at the PDR surface, the upper boundary in the present data is slightly higher (76) and $\overline{N_C}$ does not drop below 70.

With the 11.2/3.3 μm PAH band strength ratio and the quantitative measures for PAH size

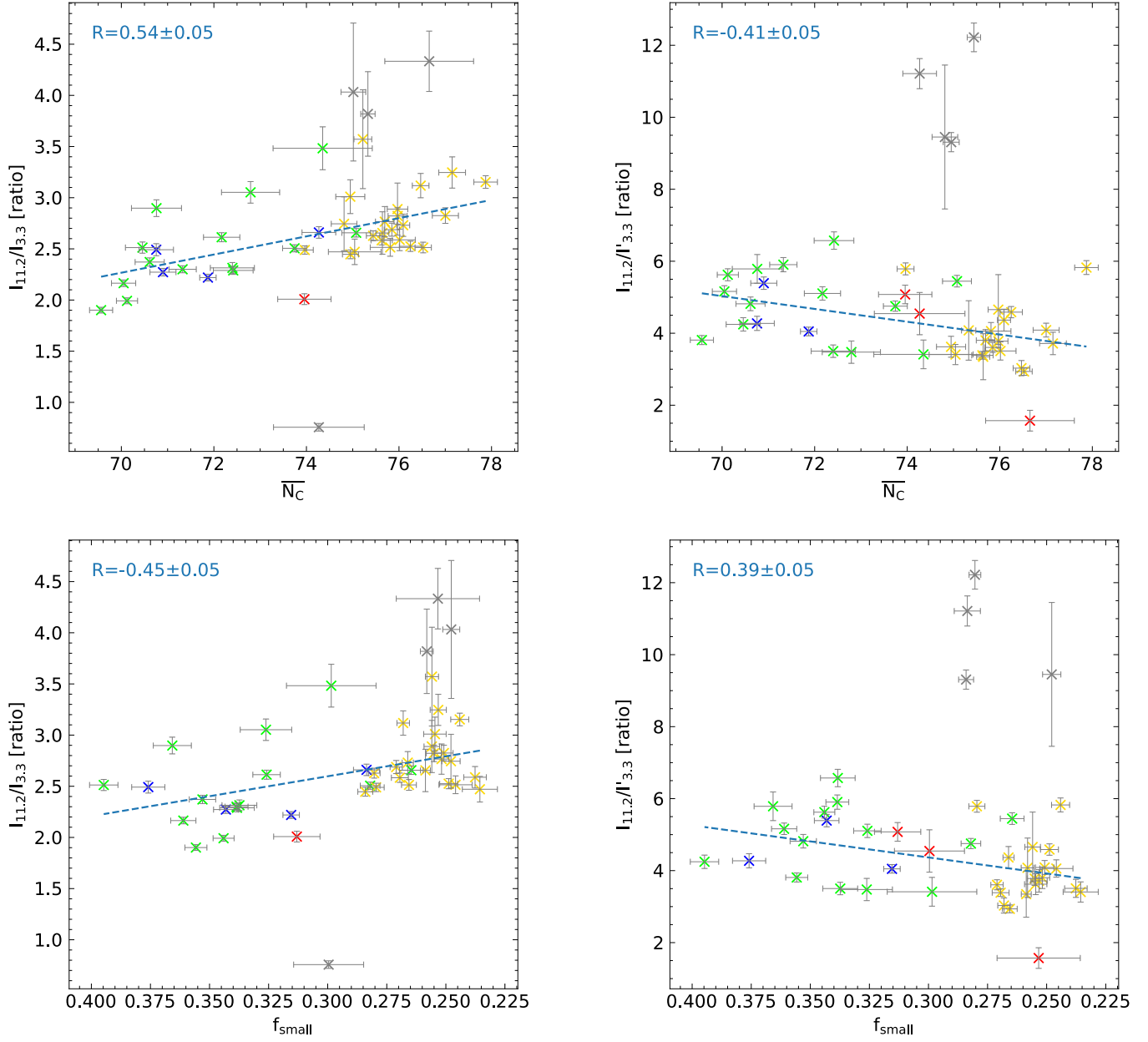


Figure 9. PAH band strength ratio and PAHdb-derived size correlations. The top two panels present the 11.2/3.3 μm PAH band strength ratio against the PAHdb-determined average number of carbon atoms ($\overline{N_C}$) whilst the bottom two panels that versus the small PAH fraction f_{small} ($N_C \leq 50$). Panels to the left and right use the 3.3 μm PAH band strength determined through direct integration ($I_{3.3}$) and spectro-photometric modeling ($I'_{3.3}$), respectively. Points are color coded according their zone as assigned in Figure 1. Clipped points are shown in gray (3σ). Uncertainties have been propagated, indicated as gray error bars, and data points with a SNR less than three have been discarded. Given is the weighted Pearson correlation coefficient R (blue) for a straight line (dashed). See Section 4.5 for details.

from PAHdb, correlating one with the other has the potential to provide a direct calibrator for PAH size. This is analogous to what has been done for PAH charge, where the 6.2/11.2 μm PAH band strength ratio is correlated with the PAHdb-derived PAH cation/neutral ratio, which, in turn, is connected to the PAH ionization parameter (γ ; e.g., F. Galliano et al. 2008; C. Boersma et al. 2018; A. Maragkoudakis et al. 2022).

The top two panels of Figure 9 present 11.2/3.3 versus $\overline{N_C}$. In the left and right panel the 3.3 μm PAH band strength determined through direct integration ($I_{3.3}$) and spectrophotometric modeling ($I'_{3.3}$) are shown, respectively. With a sigma-clip of 3σ and disregarding points with a signal-to-noise ratio (SNR) of less than 3, a tentative, slightly positive trend appears ($R=0.54\pm0.05$) for the former. However, use of $I'_{3.3}$ reveals a less convincing negative correlation ($R=-0.41\pm0.05$). This behavior is driven by $I'_{3.3}$ and reflects that seen in the right panel of Figure 7. Moreover, the range in $\overline{N_C}$ is very limited, spanning only ~ 6 carbon atoms, despite $I_{11.2}/I'_{3.3}$ covering much of the observed astronomical variation ($\sim 4\text{-}7$; e.g., A. Maragkoudakis et al. 2020). In addition, careful analysis of JWST observations of the Orion Bar with PAHdb are able to recover the expected trend, albeit after averaging a large number of points (A. Maragkoudakis et al. *under review*). Section 4.4 provides possible explanations for the discrepancy seen here.

In the bottom two panels of Figure 9 11.2/3.3 versus f_{small} is considered. As with $\overline{N_C}$, f_{small} shows a tentative trend when using $I_{3.3}$ ($R=-0.45\pm0.05$) and a less convincing one with $I'_{3.3}$ ($R=0.39\pm0.05$). The range in f_{small} is relatively small, only spanning ~ 0.14 . In contrast, the range in the PAHdb-derived PAH cation fraction is almost three times larger (~ 0.41) and remains above ~ 0.60 throughout the FOV.

On top of the possible reasons given in Section 4.4, it could be that the intrinsic intensity of the C-H stretches and bends is a contributing factor for not observing stronger correlations. That is, C-H stretches and bends are significantly stronger in neutral PAHs than their ionized counterparts. With larger PAHs more readily being ionized, and since the environment is highly ionized, the 11.2/3.3 μm PAH band strength ratio might not fully capture the subpopulation of large ionized PAHs.

Another possibility is that the ongoing photochemistry does not allow for a straightforward interpretation of PAH size, certainly not as easily as has been the case for PAH charge. Perhaps this is related to how the assorted population of freshly minted PAHs sublimated off icy grains entering the diffuse medium at the PDR-front is steadily evolving toward one of mainly fullerenes when approaching HD200775 (O. Berné & A. G. G. M. Tielens 2012; O. Berné et al. 2013). A larger, more varied sample of sizable extended objects of combined SPHEREx and Spitzer spectral mapping observations will be needed to provide stronger evidence for the reported trends.

On the database fitting side, directly including the 3.3 μm PAH feature could provide an additional constraint that might break, if present, any size degeneracy and alter the trends favorably. However, this is not straightforward due to the spectral complexity of the 3-5 μm region (see e.g., C. Boersma et al. 2023; D. Van De Putte et al. 2025). Moreover, the picture painted thus far already aligns with that of rapid photo-alteration of the population as soon as the PAHs leave the dense medium and larger PAHs becoming more prominent members when moving through the diffuse medium closer toward HD200775.

5. CONCLUSIONS

The following conclusions are drawn:

1. Observations by the SpectroPhotometer for the History of the Universe, Epoch of Reionization, and Ices Explorer (SPHEREx) of the Galactic interstellar medium enable the study of the aromatic and aliphatic evolution across large extended objects by providing extraordinary access to the 3.3 polycyclic aromatic hydrocarbon (PAH) and 3.4 μm aliphatic features, respectively.
2. The 3.3 and 3.4 μm emission in the northwest PDR of NGC7023 peaks at the PDR-front, both dropping off when moving into the diffuse medium in the direction of the irradiating star, HD200775, located toward the south-east, and when moving into the direction of the embedded young stellar object in the northwestern corner of the field-of-view (FOV).
3. The 3.4/3.3 μm band strength ratio in NGC7023 shows a demarcation that matches the large-scale morphology of the region, which, in turn, is consistent with an interpretation that PAH superhydrogenation and aliphatic side groups are able to survive in more shielded regions but get quickly removed when entering the unshielded, diffuse medium. This demarcation shows up as two distinct trends when plotting the 3.4 versus the 3.3 μm band strength, one associated with the dense medium and the other with the diffuse medium; $[N_{\text{H,ali}}/N_{\text{H,aro}}]_{\text{dense}} = 0.42 \pm 0.01$ and $[N_{\text{H,ali}}/N_{\text{H,aro}}]_{\text{diffuse}} = 0.01 \pm 0.01$.
4. In conjunction with matching Spitzer spectral map observations, SPHEREx enables the study of the PAH size evolution across large extended objects by providing access to the 3.3 μm PAH band that, when ratioed against the 11.2 μm PAH band, is considered the primary observational tracer for PAH size.
5. The 11.2/3.3 μm PAH band strength ratio in NGC7023 also follows the large-scale morphology of the region, with the same demarcation. Here, this is consistent with an interpretation that the smaller PAHs in the population are quickly whittled away when entering the more exposed, diffuse medium. However, this is only the case when considering the 3.3–3.4 μm complex and not so when it is decomposed into a separate 3.3 and 3.4 μm sub-feature.
6. NASA Ames PAH IR Spectroscopic Database Monte Carlo fits to the isolated $\sim 5\text{--}15\ \mu\text{m}$ Spitzer PAH spectra to retrieve the average number of carbon atoms ($\overline{N_{\text{C}}}$) and small PAH fraction (f_{small} ; $N_{\text{C}} \leq 50$) are able to pick up the demarcation between the dense and diffuse medium, with $\overline{N_{\text{C}}}$ increasing and f_{small} decreasing toward HD200775, respectively. This is despite little variation across the FOV; $70 \lesssim \overline{N_{\text{C}}} \lesssim 76$ and $0.24 \lesssim f_{\text{small}} \lesssim 0.36$.
7. The 11.2/3.3 PAH band strength ratio versus $\overline{N_{\text{C}}}$ and f_{small} , show tentative correlations ($R=0.54 \pm 0.05$ and -0.45 ± 0.05 , respectively). Once again, this is only the case when considering the 3.3–3.4 μm complex. In the case of the 3.3 μm PAH band strength from the decomposed complex, the correlations are flipped and less tight with $R=-0.41 \pm 0.05$ and 0.39 ± 0.05 for $\overline{N_{\text{C}}}$ and f_{small} , respectively.
8. Studying a sample of various large(r) extended objects with varying astrophysical and astrochemical conditions is needed to put the reported trends on a stronger footing, tighten the correlations, and turn the 11.2/3.3 μm into a quantitative calibrator for PAH size. Moreover, it will expose the reason for the discrepancy between the results when considering the 3.3–3.4 μm complex as a whole and the decomposed 3.3 μm sub-feature on its own.

ACKNOWLEDGMENTS

This publication makes use of data products from the Spectro-Photometer for the History of

the Universe, Epoch of Reionization and Ices Explorer (SPHEREx), which is a joint project of the Jet Propulsion Laboratory and the California Institute of Technology, and is funded by the National Aeronautics and Space Administration (NASA). In addition, this work is based in part on observations made with the Spitzer Space Telescope, which was operated by the Jet Propulsion Laboratory, California Institute of Technology under a contract with NASA. C.B. is grateful for an appointment at NASA Ames Research Center through the San José State University Research Foundation (80NSSC22M0107). L.J.A., A.M., and J.D.B. are thankful for an appointment at NASA Ames Research Center through the Bay Area Environmental Research Institute (80NSSC23M0028). R.C.F. acknowledges funding support from NASA Grant 80NSSC24M0132. C.B., A.M., L.J.A., J.D.B., P.T., V.J.E., and R.C.F. acknowledge support from the Internal Scientist Funding Model (ISFM) Laboratory Astrophysics Directed Work Package at NASA Ames.

AUTHOR CONTRIBUTIONS

C.B. was responsible for conceptualization, data curation, formal analysis, investigation, methodology, project administration, validation, visualization, and writing; both the original draft and during review & editing. A.M. aided with the methodology. A.M., L.J.A., J.D.B., P.T., V.J.E., and R.C.F. were responsible for validation and writing; both the original draft as well as during review & editing.

Facilities: SPHEREx, Spitzer(IRS)

Software: AmesPAHdbPythonSuite (The PAHdb Team 2022), astropy (Astropy Collaboration et al. 2013, 2018, 2022), photutils (L. Bradley et al. 2025), pyphot (M. Fouesneau 2025)

REFERENCES

Allamandola, L. J., Tielens, A. G. G. M., & Barker, J. R. 1989, *ApJS*, 71, 733, doi: [10.1086/191396](https://doi.org/10.1086/191396)

Astropy Collaboration, Robitaille, T. P., Tollerud, E. J., et al. 2013, *A&A*, 558, A33, doi: [10.1051/0004-6361/201322068](https://doi.org/10.1051/0004-6361/201322068)

Astropy Collaboration, Price-Whelan, A. M., Sipőcz, B. M., et al. 2018, *AJ*, 156, 123, doi: [10.3847/1538-3881/aabc4f](https://doi.org/10.3847/1538-3881/aabc4f)

Astropy Collaboration, Price-Whelan, A. M., Lim, P. L., et al. 2022, *ApJ*, 935, 167, doi: [10.3847/1538-4357/ac7c74](https://doi.org/10.3847/1538-4357/ac7c74)

Bauschlicher, C. W., Boersma, C., Ricca, A., et al. 2010, *ApJS*, 189, 341, doi: [10.1088/0067-0049/189/2/341](https://doi.org/10.1088/0067-0049/189/2/341)

Bauschlicher, Jr., C. W., Ricca, A., Boersma, C., & Allamandola, L. J. 2018, *ApJS*, 234, 32, doi: [10.3847/1538-4365/aaa019](https://doi.org/10.3847/1538-4365/aaa019)

Berné, O., Mulas, G., & Joblin, C. 2013, *A&A*, 550, L4, doi: [10.1051/0004-6361/201220730](https://doi.org/10.1051/0004-6361/201220730)

Berné, O., & Tielens, A. G. G. M. 2012, *Proceedings of the National Academy of Science*, 109, 401, doi: [10.1073/pnas.1114207108](https://doi.org/10.1073/pnas.1114207108)

Berné, O., Joblin, C., Deville, Y., et al. 2007, *A&A*, 469, 575, doi: [10.1051/0004-6361:20066282](https://doi.org/10.1051/0004-6361:20066282)

Bernstein, M. P., Elsila, J. E., Dworkin, J. P., et al. 2002, *ApJ*, 576, 1115, doi: [10.1086/341863](https://doi.org/10.1086/341863)

Bernstein, M. P., Sandford, S. A., & Allamandola, L. J. 1996, *ApJ Lett*, 472, L127, doi: [10.1086/310376](https://doi.org/10.1086/310376)

Bernstein, M. P., Sandford, S. A., Allamandola, L. J., et al. 1999, *Sci*, 283, 1135, doi: [10.1126/science.283.5405.1135](https://doi.org/10.1126/science.283.5405.1135)

Boersma, C., Bregman, J., & Allamandola, L. J. 2014a, *ApJ*, 795, 110, doi: [10.1088/0004-637X/795/2/110](https://doi.org/10.1088/0004-637X/795/2/110)

Boersma, C., Bregman, J., & Allamandola, L. J. 2015, *ApJ*, 806, 121, doi: [10.1088/0004-637X/806/1/121](https://doi.org/10.1088/0004-637X/806/1/121)

Boersma, C., Bregman, J., & Allamandola, L. J. 2016, *ApJ*, 832, 51, doi: [10.3847/0004-637X/832/1/51](https://doi.org/10.3847/0004-637X/832/1/51)

Boersma, C., Bregman, J., & Allamandola, L. J. 2018, *ApJ*, 858, 67, doi: [10.3847/1538-4357/aabcbe](https://doi.org/10.3847/1538-4357/aabcbe)

Boersma, C., Bregman, J. D., & Allamandola, L. J. 2013, *ApJ*, 769, 117, doi: [10.1088/0004-637X/769/2/117](https://doi.org/10.1088/0004-637X/769/2/117)

Boersma, C., Bauschlicher, C. W., Ricca, A., et al. 2014b, *ApJS*, 211, 8, doi: [10.1088/0067-0049/211/1/8](https://doi.org/10.1088/0067-0049/211/1/8)

Boersma, C., Allamandola, L. J., Esposito, V. J., et al. 2023, *ApJ*, 959, 74, doi: [10.3847/1538-4357/ad022b](https://doi.org/10.3847/1538-4357/ad022b)

Bradley, L., Sipőcz, B., Robitaille, T., et al. 2025, *astropy/photutils*: 2.2.0, 2.2.0 Zenodo, doi: [10.5281/zenodo.14889440](https://doi.org/10.5281/zenodo.14889440)

Cheng, Y.-T., Hensley, B. S., & Lai, T. S. Y. 2025, arXiv e-prints, arXiv:2506.13863, doi: [10.48550/arXiv.2506.13863](https://doi.org/10.48550/arXiv.2506.13863)

Chiar, J. E., & Tielens, A. G. G. M. 2006, *ApJ*, 637, 774, doi: [10.1086/498406](https://doi.org/10.1086/498406)

Crill, B. P., Werner, M., Akeson, R., et al. 2020, in Society of Photo-Optical Instrumentation Engineers (SPIE) Conference Series, Vol. 11443, Space Telescopes and Instrumentation 2020: Optical, Infrared, and Millimeter Wave, ed. M. Lystrup & M. D. Perrin, 114430I, doi: [10.1117/12.2567224](https://doi.org/10.1117/12.2567224)

Croiset, B. A., Candian, A., Berné, O., & Tielens, A. G. G. M. 2016, *A&A*, 590, A26, doi: [10.1051/0004-6361/201527714](https://doi.org/10.1051/0004-6361/201527714)

Draine, B. T., Li, A., Hensley, B. S., et al. 2021, *ApJ*, 917, 3, doi: [10.3847/1538-4357/abff51](https://doi.org/10.3847/1538-4357/abff51)

Esposito, V. J., Allamandola, L. J., Boersma, C., et al. 2023, *Molecular Physics*, 122, e2252936, doi: [10.1080/00268976.2023.2252936](https://doi.org/10.1080/00268976.2023.2252936)

Esposito, V. J., Bejaoui, S., Billinghamurst, B. E., et al. 2024, *MNRAS*, 535, 3239, doi: [10.1093/mnras/stae2588](https://doi.org/10.1093/mnras/stae2588)

Fouesneau, M. 2025, *pyphot*, *pyphot_v1.6.0* Zenodo, doi: [10.5281/zenodo.14712174](https://doi.org/10.5281/zenodo.14712174)

Galliano, F., Madden, S. C., Tielens, A. G. G. M., Peeters, E., & Jones, A. P. 2008, *apj*, 679, 310, doi: [10.1086/587051](https://doi.org/10.1086/587051)

Gardner, J. P., Mather, J. C., Clampin, M., et al. 2006, *Space Sci. Rev.*, 123, 485, doi: [10.1007/s11214-006-8315-7](https://doi.org/10.1007/s11214-006-8315-7)

Houck, J. R., Roellig, T. L., van Cleve, J., et al. 2004, *ApJS*, 154, 18, doi: [10.1086/422878](https://doi.org/10.1086/422878)

Khan, B., Daza Rodriguez, S. A., Peeters, E., et al. 2025, arXiv e-prints, arXiv:2510.06167. <https://arxiv.org/abs/2510.06167>

Li, A., & Draine, B. T. 2001, *apj*, 554, 778, doi: [10.1086/323147](https://doi.org/10.1086/323147)

Li, A., & Draine, B. T. 2012, *ApJ Lett*, 760, L35, doi: [10.1088/2041-8205/760/2/L35](https://doi.org/10.1088/2041-8205/760/2/L35)

Mackie, C. J., Chen, T., Candian, A., Lee, T. J., & Tielens, A. G. G. M. 2018, *jcp*, 149, 134302, doi: [10.1063/1.5038725](https://doi.org/10.1063/1.5038725)

Maragkoudakis, A., Boersma, C., Temi, P., Bregman, J. D., & Allamandola, L. J. 2022, *ApJ*, 931, 38, doi: [10.3847/1538-4357/ac666f](https://doi.org/10.3847/1538-4357/ac666f)

Maragkoudakis, A., Boersma, C., Temi, P., et al. 2025, *ApJ*, 979, 90, doi: [10.3847/1538-4357/ad9918](https://doi.org/10.3847/1538-4357/ad9918)

Maragkoudakis, A., Peeters, E., & Ricca, A. 2020, *MNRAS*, 494, 642, doi: [10.1093/mnras/staa681](https://doi.org/10.1093/mnras/staa681)

Maragkoudakis, A., Peeters, E., Ricca, A., & Boersma, C. 2023, *mn*, 524, 3429, doi: [10.1093/mnras/stad2062](https://doi.org/10.1093/mnras/stad2062)

Maragkoudakis, A., Boersma, C., Peeters, E., et al. under review, *ApJ*, 0, 0, doi: [10.3847/0/0](https://doi.org/10.3847/0/0)

Mattiola, A. L., Hudgins, D. M., Boersma, C., et al. 2020, *ApJS*, 251, 22, doi: [10.3847/1538-4365/abc2c8](https://doi.org/10.3847/1538-4365/abc2c8)

Mendoza-Gomez, C. X., de Groot, M. S., & Greenberg, J. M. 1995, *A&A*, 295, 479

Millan-Gabet, R., Schloerb, F. P., & Traub, W. A. 2001, *ApJ*, 546, 358, doi: [10.1086/318239](https://doi.org/10.1086/318239)

Misselt, K., Witt, A. N., Gordon, K. D., et al. 2025, *A&A*, 700, A158, doi: [10.1051/0004-6361/202554851](https://doi.org/10.1051/0004-6361/202554851)

Pilleri, P., Montillaud, J., Berné, O., & Joblin, C. 2012, *A&A*, 542, A69, doi: [10.1051/0004-6361/201015915](https://doi.org/10.1051/0004-6361/201015915)

Ricca, A., Roser, J. E., Boersma, C., Peeters, E., & Maragkoudakis, A. 2024, *ApJ*, 968, 128, doi: [10.3847/1538-4357/ad4151](https://doi.org/10.3847/1538-4357/ad4151)

Rogers, C., Heyer, M. H., & Dewdney, P. E. 1995, *ApJ*, 442, 694, doi: [10.1086/175475](https://doi.org/10.1086/175475)

Rosenberg, M. J. F., Berné, O., Boersma, C., Allamandola, L. J., & Tielens, A. G. G. M. 2011, *A&A*, 532, A128, doi: [10.1051/0004-6361/201016340](https://doi.org/10.1051/0004-6361/201016340)

Sandford, S. A., Bernstein, M. P., & Materese, C. K. 2013, *apjs*, 205, 8, doi: [10.1088/0067-0049/205/1/8](https://doi.org/10.1088/0067-0049/205/1/8)

SPHEREx Team. 2025, SPHEREx Quick Release Spectral Images - QR2, IPAC,
doi: [10.26131/IRSA652](https://doi.org/10.26131/IRSA652)

Spilker, J., Phadke, K. A., Aravena, M., et al. 2023, *Nature*, 618, 708,
doi: [10.1038/s41586-023-05998-6](https://doi.org/10.1038/s41586-023-05998-6)

Stock, D. J., Choi, W. D.-Y., Moya, L. G. V., et al. 2016, *ApJ*, 819, 65,
doi: [10.3847/0004-637X/819/1/65](https://doi.org/10.3847/0004-637X/819/1/65)

The PAHdb Team. 2022,
AmesPAHdbPythonSuite, Zenodo,
doi: [10.5281/ZENODO.1742858](https://doi.org/10.5281/ZENODO.1742858)

Tielens, A. G. G. M. 2008, *ARA&A*, 45, 289,
doi: [10.1146/annurev.astro.46.060407.145211](https://doi.org/10.1146/annurev.astro.46.060407.145211)

Van De Putte, D., Peeters, E., Gordon, K. D., et al. 2025, *A&A*, 701, A111,
doi: [10.1051/0004-6361/202554991](https://doi.org/10.1051/0004-6361/202554991)

van den Ancker, M. E., The, P. S., Tjin A Djie, H. R. E., et al. 1997, *A&A*, 324, L33,
doi: [10.1007/978-94-011-5468-0_18](https://doi.org/10.1007/978-94-011-5468-0_18)

Werner, M. W., Roellig, T. L., Low, F. J., et al. 2004, *ApJS*, 154, 1, doi: [10.1086/422992](https://doi.org/10.1086/422992)

Yang, X. J., Glaser, R., Li, A., & Zhong, J. X. 2017, *New Astron. Rev.*, 77, 1,
doi: [10.1016/j.newar.2017.01.001](https://doi.org/10.1016/j.newar.2017.01.001)

Yang, X. J., & Li, A. 2023, *ApJS*, 268, 50,
doi: [10.3847/1538-4365/acebe6](https://doi.org/10.3847/1538-4365/acebe6)

Yang, X. J., Li, A., & Glaser, R. 2020, *ApJS*, 247, 1, doi: [10.3847/1538-4365/ab67b6](https://doi.org/10.3847/1538-4365/ab67b6)

Young, E. T., Becklin, E. E., Marcum, P. M., et al. 2012, *ApJ Lett*, 749, L17,
doi: [10.1088/2041-8205/749/2/L17](https://doi.org/10.1088/2041-8205/749/2/L17)

Zhang, E., Faisst, A. L., Crill, B. P., et al. 2025, *ApJ*, 992, 3, doi: [10.3847/1538-4357/adfd5a](https://doi.org/10.3847/1538-4357/adfd5a)

APPENDIX

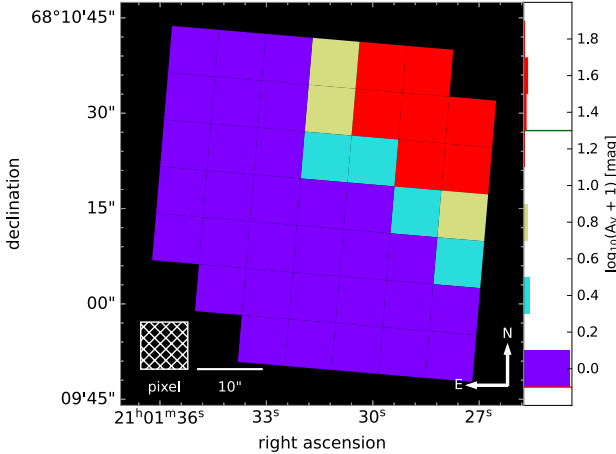


Figure A1. Visual extinction (A_V) across the northwest PDR in NGC7023. The color scale uses a 4% cutoff on the high and a 1% cutoff on the low end, indicated by the green and red lines in the color bar, respectively. This suppresses outliers. See Appendix A for details.

A. EXTINCTION CORRECTION

Spectra have been corrected for extinction. The visual extinction (A_V) determined by C. Boersma et al. (2018) is taken, which was derived using the Galactic center extinction curve from J. E. Chiar & A. G. G. M. Tielens (2006). See C. Boersma et al. (2018) for additional detail. Figure A1 presents a map of the visual extinction, resampled onto the SPHEREx FOV.

B. SPLICING

As there is no overlap between the SPHEREx and Spitzer segments, they cannot be directly spliced together. Therefore, the predicted and observed IRAC photometry are used to scale the SPHEREx segment per:

$$\frac{SF \cdot \text{IRAC1}_{\text{predicted}}}{\text{IRAC4}_{\text{predicted}}} = \frac{\text{IRAC1}_{\text{observed}}}{\text{IRAC4}_{\text{observed}}}. \quad (\text{B1})$$

Figure B2 presents a map of the derived scaling factors SF . Since SF scales the relative photometric bands, no assessment is made

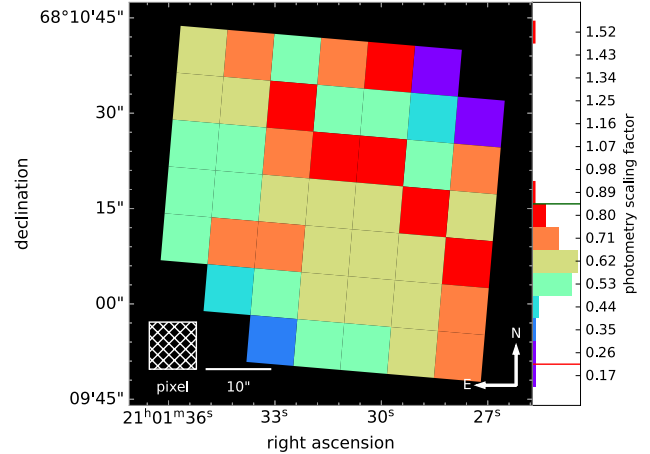


Figure B2. SPHEREx segment scaling factors across the northwest PDR in NGC7023 determined from predicted and actual IRAC channel 1 and 4 photometry. The color scale uses a 4% cutoff on the high and a 1% cutoff on the low end, indicated by the green and red lines in the color bar, respectively. This suppresses outliers. See Appendix B for details.

on the absolute flux calibration of either the SPHEREx or Spitzer segments. Given that this is a single multiplicative factor, scaling factors are applied to the SPHEREx band strength measurements and not to the segment as a whole before the analysis.

C. SPECTRO-PHOTOMETRIC MODEL

The model used in Section 3.2 to reproduce the SPHEREx bandpass-integrated spectro-photometry solves for:

$$F_{\lambda, \text{SPHEREx}} \Delta \lambda_{\text{SPHEREx}} - \int_{\Delta \lambda_{\text{SPHEREx}}} F_{\lambda, \text{model}}(\lambda) d\lambda = 0, \quad (\text{C2})$$

where $F_{\lambda, \text{SPHEREx}}$ is the photometric data point in $\text{W cm}^{-2} \mu\text{m}^{-1}$, $\Delta \lambda_{\text{SPHEREx}}$ the bandpass in μm , and $F_{\lambda, \text{model}}(\lambda)$ the model spectrum with units of $\text{W cm}^{-2} \mu\text{m}^{-1}$. The integration of $F_{\lambda, \text{model}}(\lambda)$ is done over the bandpass $\Delta \lambda_{\text{SPHEREx}}$.

$F_{\lambda,\text{model}}(\lambda)$ consists of two blended Gaussian profiles that describe the 3.29 and 3.4 μm features, respectively, and a straight baseline:

$$F_{\lambda,\text{model}}(\lambda) = m\lambda + b + \sum_{i=1}^2 G_{\lambda,i}(\lambda) , \quad (\text{C3})$$

where m and b are the slope and offset of the straight baseline, respectively. $G_{\lambda,i}(\lambda)$ represent the Gaussian profile:

$$G_{\lambda,i}(\lambda) = A_i e^{-\frac{(\lambda - \lambda_{0,i})^2}{2\sigma_i^2}} , \quad (\text{C4})$$

where A_i , $\lambda_{0,i}$, and σ_i stand for the center flux in $\text{W cm}^{-2} \mu\text{m}^{-1}$, center wavelength in μm , and width in μm , respectively. The band strength $G_{\lambda,i}$ is then determined as

$$G_{\lambda,i} = A_i \sigma_i \cdot \sqrt{2\pi} . \quad (\text{C5})$$

A_i is forced strictly positive, line centers $\lambda_{0,i}$ are set to 3.279 and 3.40 μm , and widths to 0.0247 and 0.0807 μm for the 3.3 and 3.4 μm components, respectively. Line centers are allowed to vary within 0.04 μm and the widths σ_i between 0.02 and 0.3 and 0.07 and 0.09 μm for the 3.3 and 3.4 μm components, respectively. Uncertainties are propagated.